EES Catalysis

PAPER

View Article Online
View Journal | View Issue

Cite this: *EES Catal.*, 2025, 3, 446

High-performance and stable NH_3 production using a TiO_2-protected Si photocathode and patterned Au loading†

Ahmad Tayyebi, ‡*[ae] Jeong Juyeon,‡[a] Mahsa Haddadi Moghaddam, ‡[b] Mohammad Zafari, ‡[c] Hyun-ju Go,[a] Dukhyung Lee,[b] Meysam Tayebi,[d] Hwa-Young Yang,[a] Changhwan Shin,[a] Maria del Carmen Gimenez-Lopez,[e] Geunsik Lee, *[c] Dai Sik Kim*[b] and Ji-Wook Jang *[afg]

Received 16th December 2024,
Accepted 2nd January 2025

DOI: 10.1039/d4ey00282b

rsc.li/eescatalysis

Crystalline silicon (c-Si) is a promising material for photoelectrochemical (PEC) ammonia (NH_3) production from nitrate (NO_3^-) reduction owing to its appropriate band gap and optimal charge-transport properties. However, c-Si is not stable in aqueous solutions, causing the detachment of catalysts from the c-Si photoelectrode and resulting in a dramatic decrease in the performance. Furthermore, electrocatalysts on c-Si block light, therby reducing the PEC NH_3-production efficiency. Herein, we stabilized and increased the efficiency of the c-Si photocathode by TiO_2 deposition and loaded an optimized amount of Au using an e-beam patterning, respectively. We found that TiO_2 not only protects the c-Si photoelectrode from the electrolyte but also promotes strong bonding between Au and the c-Si photoelectrode. Notably, TiO_2 showed a synergistic effect with the Au electrocatalyst in increasing the faradaic efficiency (FE) of NO_3^- reduction for NH_3 production, which was further confirmed by density functional theory calculations. Overall, the Au-loaded TiO_2-protected c-Si photoelectrode showed a stable and record-high NH_3-production rate of 1590 ± 40 μg_{NH_3} cm^{-2} h^{-1} with an FE of 83.4% ± 5.6% at −0.35 V *vs.* the reversible hydrogen electrode.

Broader context

Developing a photoelectrochemical (PEC) device for the conversion of nitrate to ammonia is a promising approach for decentralized ammonia production and sustainable wastewater treatment process. In this work, we developed a highly stable and high-performance photocathode by depositing a gold (Au) pattern on the surface of a silicon (c-Si) wafer using a photolithography technique for NH_3 production. Our photoelectrode exhibited a record-high NH_3-production rate of 1590 ± 40 μg_{NH_3} cm^{-2} h^{-1} with an 83.4% ± 5.6% faradaic efficiency (FE) and stable long-term operation under 44 h continuous illumination. The high production rate of the Si–TiO_2–Au photocathode can be attributed to the role of the Au pattern in circumventing the rate-determining step (RDS) in NO_3^- reduction ($NO_3^- \rightarrow NO_2^-$) and the excellent catalytic role of the ALD-TiO_2 layer in NH_3 production. The synergistic effect of Au and TiO_2 could be scaled up through photolithography. This offers a promising photocathode for the PEC conversion of nitrate ions into ammonia.

[a] *School of Energy and Chemical Engineering, Ulsan National Institute of Science and Technology (UNIST), Ulsan 44919, Republic of Korea. E-mail: ahmad.tayyebi@usc.es, jiwjang@unist.ac.kr*
[b] *Department of Physics, Ulsan National Institute of Science and Technology (UNIST), Ulsan 44919, Republic of Korea. E-mail: daisikkim@unist.ac.kr*
[c] *Department of Chemistry, Ulsan National Institute of Science and Technology (UNIST), Ulsan 44919, Republic of Korea. E-mail: gslee@unist.ac.kr*
[d] *Advanced Industrial Chemistry Research Center, Advanced Convergent Chemistry Division, Korea Research Institute of Chemical Technology (KRICT), 45 Jonggaro, Ulsan 44412, Republic of Korea*
[e] *Centro Singular de Investigación en Química Biológica y Materiales Moleculares (CIQUS), Universidad de Santiago de Compostela, 15782, Spain*
[f] *Graduate School of Carbon Neutrality, Ulsan National Institute of Science and Technology (UNIST), Ulsan 44919, Republic of Korea*
[g] *Emergent Hydrogen Technology R&D Centre, Ulsan National Institute of Science and Technology (UNIST), Ulsan 44919, Republic of Korea*

† Electronic supplementary information (ESI) available. See DOI: https://doi.org/10.1039/d4ey00282b

‡ These authors contributed equally to this work.

1. Introduction

The exponential growth in the global population over the past two decades has posed significant challenges to the expansion of food production.[1,2] Nitrogen-based fertilizers, which primarily rely on ammonia (NH_3) that comprises 80% of these fertilizers by volume serve as the primary source of nutrition for the agricultural produce within the food supply chain.[3,4] Additionally, NH_3 offers promise as an energy carrier owing to its notably high volumetric energy density (15.6 MJ L^{-1}), surpassing that of Li-ion batteries (1.73 MJ L^{-1}) and compressed H_2 (5.5 MJ L^{-1} at 70 MPa).[3–6] NH_3 is predominantly produced using the energy-intensive Haber–Bosch (HB) process that operates under high temperature and pressure over 250 °C and 300 atm, respectively.[7,8] This process accounts for more than 1–2% of the world's energy consumption and 1.6% of worldwide CO_2 emissions.[7,9] Hence, recent efforts have been dedicated to developing more energy-efficient and less CO_2-emitting methods for NH_3-production processes.[10–14] Photoelectrochemical (PEC) NH_3 production is a promising technique, because it can be operated at ambient temperature and pressure without the need for expensive H_2 and without emitting CO_2.[15,16]

Crystalline silicon (c-Si) is a promising material for PEC NH_3 production because it can absorb a wide range of the solar spectrum due to its small band gap of 1.1 eV and high carrier mobility.[17–19] Recently, several works have reported on the application of c-Si photoelectrodes for the PEC nitrogen (N_2)-reduction reaction (NRR).[20–23] For example, MacFarlane *et al.* utilized Au-electrocatalyst-loaded c-Si and achieved an NH_3-production rate of 1.33 μg_{NH_3} cm^{-2} h^{-1} under 2 suns illumination.[20] Zheng *et al.* applied the aerophilic polytetrafluoroethylene (PTFE) to a Au-loaded c-Si photocathode to increase the Faraday efficiency (FE) for the NRR, and achieved a NH_3-production rate of ~18.9 μg cm^{-2} h^{-1} with 37.8% NH_3 selectivity at −0.2 V *vs.* the reversible hydrogen electrode (RHE).[24]

To commercialize PEC NH_3 production, the NH_3-production rate needs to be more than ~1000 μg NH_3 cm^{-2} h^{-1}, which is equivalent to a current density of approximately 10 mA cm^{-2}.[25,26] However, the NRR partial current density in aqueous electrolytes is usually less than 1 mA cm^{-2}, which correspond to less than a 100 μg NH_3 cm^{-2} h^{-1} NH_3 production rate (about 10-times lower compared to the NO_3-reduction reaction), because less N_2 (0.0001 M) is dissolved in the water and N≡N bonds are hard to selectively dissociate.[27,28] Replacing N_2 with nitrate (NO_3^-) as a nitrogen-containing source can address some of the drawbacks of the NRR, because NO_3^- is very soluble in water (0.5–2 M) and NO_3^- can be easily converted into NH_3 through nitrite (NO_2^-) with a high FE.[2] Thus NH_3 production from NO_3^- may be a promising way to not only maximize the NH_3 productivity but also for the remediation of NH_3 from waste streams and seawater.[29]

Lee *et al.* used Au-decorated c-Si nanowires for the PEC reduction of NO_3^- to NH_3, achieving a high NH_3 FE of 95.6% at a positive applied potential (0.2 V *vs.* RHE).[16] However, the NH_3-production rate remained very low (>10 μg_{NH_3} h^{-1} cm^{-2}), and both the FE and NH_3-production rate gradually decreased due to the detachment of Au nanoparticles (NPs) from the electrode surface.[16] Au-loaded c-Si photocathodes showed low stability and performance for PEC NH_3 production, due to the severe photocorrosion and chemical etching of the c-Si photoelectrode, especially in alkaline media. The continuous etching of c-Si in the corrosive electrolyte not only diminished its performance but also led to the detachment of the electrocatalyst from the photoelectrode.[16]

In the present study, we demonstrated high-performance and stable NH_3 production by protecting the c-Si photocathode with a TiO_2 layer deposited by atomic layer deposition (ALD), followed by patterned Au deposition. The TiO_2 layer could not only protect the c-Si surface from electrolyte degradation, but could also improve the adhesion between the Au catalyst and the Si. By optimizing the amount of Au loading through the photolithography technique, we were able to minimize the light absorption by the Au catalyst while maintaining a high selectivity for NH_3 production. Our Au-loaded TiO_2 protected c-Si photocathode (Si/TiO_2/Au) exhibited a record-high production rate of 1590 ± 40 μg_{NH_3} cm^{-2} h^{-1}, which is higher than the NH_3-production rate criteria for the practical application of PEC NH_3 production. Moreover, the FE of NH_3 was as high as 83.4 ± 5.6%, and Si/TiO_2/Au demonstrated stability during long-term operation under 44 h continuous illumination. The high production rate of the Si/TiO_2/Au photocathode could be attributed to the role of Au in circumventing the rate-determining step (RDS) in NO_3^- reduction ($NO_3^- \rightarrow NO_2^-$) and the catalytic role of the ALD-TiO_2 layer in NH_3 production, which was further verified by density functional theory (DFT) calculations. These results indicate that TiO_2 not only protects the c-Si surface from Au electrocatalyst detachment, but also plays an important role in the selective NO_3^- reduction reaction to produce NH_3.

2. Results and discussion

2.1. Fabrication process and PEC performance of Si/TiO_2/Au

A thin layer of TiO_2 (~20 nm) was deposited on the surface of a cleaned HF-treated p-type silicon (p-Si) wafer using the ALD technique (ESI,† Fig. S1). Photolithography was conducted using a Cr photomask to print square patterns with different sizes and densities on the surface of p-Si.[30,31] After spin-coating and soft baking of the photoresist, an MIF 300 developer was used to imprint the desired pattern on the Si/TiO_2 substrate. Finally, a 100 nm metallic film (Au) was deposited by an e-beam evaporator (ESI,† Fig. S2), and the desired pattern was lifted by washing the resist in acetone solution for 60 s (Fig. 1(a)). To remove any extra photoresist, an oxygen plasma treatment was utilized to clean the photocathode surface. Fig. 1(b) and ESI,† Fig. S3 show top-view microscopy and angled scanning electron microscopy (SEM) images of the Au pattern with a 4% density on the surface of Si/TiO_2 (Si/TiO_2/Au-4). Energy-dispersive spectroscopy (EDS) elemental mapping indicated that the Au patterns, without any imperfection or missing

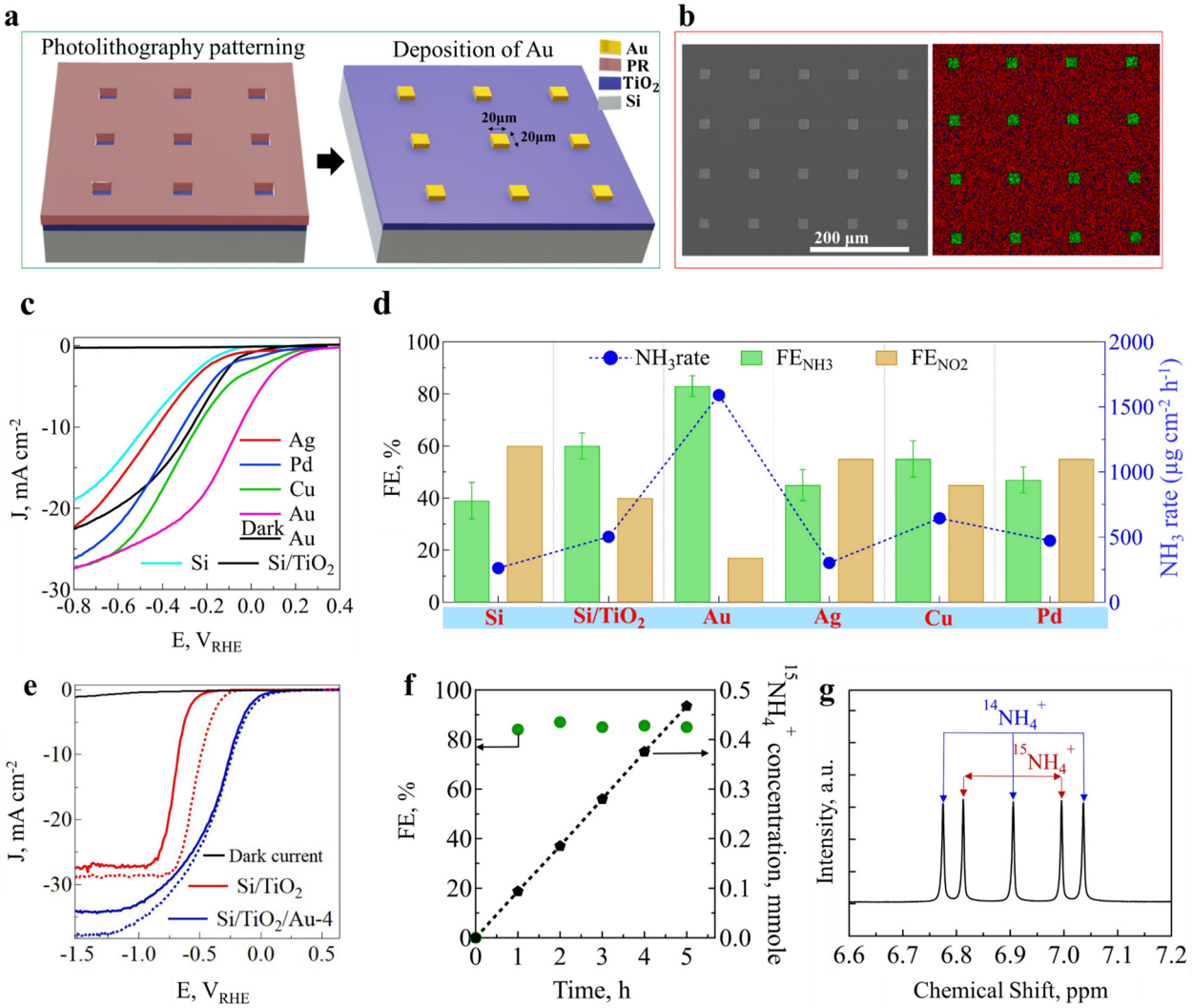

Fig. 1 (a) Schematic of the Si/TiO_2/Au-4 photocathode fabrication process. An ultrathin layer of TiO_2 was deposited on the surface of p-Si by atomic layer deposition (ALD), and then a low density 20 μm × 20 μm pattern was printed onto the Si/TiO_2 substrate using a photolithography process, and then, 100 nm Au was deposited and lifted off in acetone. (b) SEM image and elemental mapping of Au patterns on the Si/TiO_2 surface, red (Si) and green (gold). (c) *J*–*V* curves for the photocathodes for patterns with different metals in 0.5 M NO_3^- and 1.0 M KOH (pH = 14). (d) NH_3-production rates and FEs for NH_3 and NO_2^- with the Si/TiO_2/M-4 photocathode (M: Au, Pd, Cu, Ag) with different metal pattern deposition at −0.35 V *vs.* RHE after 2 h in 1.0 M KOH and 0.5 M NO_3^-, (e) *J*–*V* curves for SiTiO_2 and Si/TiO_2/Au-4 for the electrolyte containing 0.5 M KNO_3 (solid line) and KNO_2 (grid line) at pH = 14. (f) FE% and $^{15}NH_4^+$ concentration for isotopically labelled 0.5 M $^{15}NO_3^-$ as a nitrogen-containing source in 1.0 M KOH. (g) ^{1}H-NMR graphs for a control electrolyte containing the same molar ratio of $^{14}NO_3^-$ and $^{15}NO_3^-$.

squares, occupied about 4% of the photoelectrode surface, leaving 96% of the surface free for light penetration into the p-Si/TiO_2 substrate and for electron–hole generation (Fig. 1(b) and ESI,† Fig. S4). Using this photolithography method, we also loaded other patterned metals, such as Ag, Cu, and Pd, on Si/TiO_2 photoelectrode. Since Au was the most effective in the NO_3^- reduction reaction to produce NH_3, we selected Au as the main electrocatalyst (Fig. 1(c), (d), and ESI,† Fig. S5). The determined band alignments of p-Si with and without metal catalyst doping are depicted in ESI,† Fig. S6. A large downward band bending of 0.4 eV was observed for the p-Si photoelectrode without Cu or Au catalyst doping. The photogenerated electrons are transferred to the conduction band of silicon upon light irradiation. However, due to the small band gap, the photoexcited electrons recombine, likely leading to an inactive surface for NO_3^- reduction (ESI,† Fig. S6a). After Cu metal doping, the band bending was slightly decreased, resulting in an improvement in the photocurrent density and onset potential (ESI,† Fig. S6b). When Au catalyst was deposited on the surface, the Schottky barrier created due to its high work function facilitated electron transfer to the surface. This barrier reduced the backward flow of electrons from the Au to the p-Si, improving the NITRR kinetics and suppressing the recombination of photogenerated electron–hole pairs (ESI,† Fig. S6c). However, due to the weak Cu work function, some of the photogenerated electrons likely returned to p-Si, reducing the PEC performance.

We first investigated the role of the TiO_2 layer in the PEC NO_3^- reduction reaction to produce NH_3. As shown in Fig. 1(c)

and ESI,† Fig. S7a, the onset potential was shifted by 0.21 V toward a more positive potential, and the PEC performance was improved by nearly 27% for Si/TiO_2 compared to the Si photoelectrodes. Furthermore, Si/TiO_2 demonstrated a higher NH_3 FE of 60% compared to 40% for the bare Si (ESI,† Fig. S7b). Therefore, the ALD-deposited TiO_2 layer could not only protect the Si surface from chemical etching, but also improved the PEC performance and selectivity for NO_3^- reduction to NH_3. The role of Au on bare p-Si and Si/TiO_2 was also examined. In both cases, Au loading improved the onset potential and photocurrent density due to the catalytic activity of Au active sites for the reduction of NO_3^- ions (ESI,† Fig. S7a). Subsequently, with an optimized Au pattern on the TiO_2 layer, the NH_3 FE was improved to 83.4 ± 5.6%. This improvement could be attributed to the critical role of the Au pattern in converting NO_3^- to NO_2^- ions, which is well-known to be the RDS (eqn (1)).[32] To elaborate, the PEC performance was recorded for Si/TiO_2 and Si/TiO_2/Au-4 in the presence of NO_3^- and NO_2^- aqueous solutions. As shown in Fig. 1(e), the onset potential clearly shifted for Si/TiO_2 in the presence of NO_2^- compared to NO_3^-. In contrast, the onset potential and PEC performance for Si/TiO_2/Au-4 changed only slightly, indicating the crucial role of Au in suppressing the activation energy for the sluggish conversion of NO_3^- to NO_2^- in the RDS steps.[32] Element mapping of the Au pattern after 24 h continuous NO_3^- conversion to NH_3 was performed for the elements N, K, Si, and Au. As shown in ESI,† Fig. S8, only on the surface of the Au pattern were both N and K detected, corresponding to the attachment of KNO_3 on the surface, while on the Si surface these elements were missing. This clearly demonstrated the critical role of the Au pattern in the adsorption and conversion of NO_3^- ions.

Subsequently, it could be concluded that the Au pattern facilitated the sluggish 2e reduction of NO_3^- to NO_2^- (eqn (1)). In the next step (eqn (2)), intermediate NO_2^- ions are converted to NH_3 mainly on the TiO_2 surface. Therefore, the kinetics and thermodynamics of NO_3^- reduction to NH_3 (eqn (3)) are accelerated due to the synergistic effect of both the Au and TiO_2 layers, which enhances the RDS $2e^-$ reduction of NO_3^- to NO_2^- (eqn (1)) and the subsequent $6e^-$ reduction reaction to NH_3 (eqn (2)). The results and explanations above were further validated through DFT calculations, as reported in the final section.

$$NO_3^- + H_2O + 2e^- \rightarrow NO_2^- + 2OH^- \quad (1)$$

$$NO_2^- + 6H_2O + 6e^- \rightarrow NH_4OH + 7OH^- \quad (2)$$

$$NO_3^- + 7H_2O + 8e^- \rightarrow NH_4OH + 9OH^- \quad (3)$$

To elaborate the competitive reactions of the NITRR and HER, which can occur simultaneously on the photocathode surface, the performance of the Si/TiO_2/Au-4 photocathode was measured in the presence and absence of NO_3^- ions under 1 sun illumination (ESI,† Fig. S9a). The onset potential was shifted about 0.25 V toward a more positive potential in the presence of NO_3^- ions, attributed to the less thermodynamically demanding NO_3^- reduction reaction (NITRR) compared to the HER.[16] Moreover, an increased photocurrent density of about 20% was observed for the NITRR compared to that of the HER. To further assess the performance of Si/TiO_2/Au-4, we quantitatively measured the products in the cathode compartment in the presence and absence of NO_3^- ions (ESI,† Fig. S9b). For this control experiment, an H-cell configuration was used, with the catholyte connected to a gas chromatography (GC) instrument to measure the H_2 evolution. Additionally, a syringe sampling system was employed to take samples from the catholyte solution to measure the NH_3 and NO_2^- concentrations using indophenol blue and Griess procedures, respectively (ESI,† Fig. S10–S12). As shown in ESI,† Fig. S9b, in the absence of NO_3^- ions, only H_2 was evolved. In contrast, in the presence of NO_3^-, the HER reaction was effectively suppressed and NH_3 was produced continuously without H_2 gas bubbling. The influence of the product evolution during the PEC performance of Si/TiO_2/Au-4 is shown in ESI,† Fig. S9c. It can be seen an stable NH_3 production rate with no hydrogen gas evolution.

Another critical point is that we precisely identified the source of NH_3 production, attributing it to the reduction of NO_3^- ions rather than contamination (*e.g.*, NH_3 in air and human breath) or formation from other nitrogen-containing sources (*e.g.*, N_2, nitrite, amines, and nitrogen oxides, as shown in ESI,† Fig. S13). We next conducted $^{15}NO_3^-$ isotope labelling, which allowed us to carefully identify and quantify the source and amount of $^{15}NH_3$ production *via* a ^{1}H-NMR calibration curve (ESI,† Fig. S14a and b). Specifically, we observed that the ^{1}H-NMR doublet peak intensity increased over time, as shown in ESI,† Fig. S14c, leading to a consistent increase in $^{15}NH_4^+$ concentration, proving that $^{15}NO_3^-$ ions were the only source of NH_3 production (Fig. 1(f)). Furthermore, a control experiment was carried out with a mixture of $^{15}NO_3^-$ and $^{14}NO_3^-$ ions as nitrogen-containing sources. The ^{1}H-NMR spectra presented a mixed spectrum of doublet and triplet peaks attributed to the presence of $^{14}NH_4^+$ and $^{15}NH_4^+$ (Fig. 1(g)).

2.2. Optimization of the Au loading amount on Si/TiO_2

As depicted in ESI,† Fig. S15, an optimal surface coverage by the Au pattern is critical for NH_3 production. When only a small portion of the photoelectrode's surface was covered by the Au pattern, the reduction of NO_3^- to NH_3 was not efficient; while when the coverage percentage of Au was too high, Au blocked the light, resulting in a dramatic loss in PEC performance (ESI,† Fig. S15). Thus, we optimized the amount of the Au in Si/TiO_2/Au-*X* (*X* = 0.0, 0.5, 4.0, 25, 50, 100) photocathodes (*X* correlates to the surface percentage of the photoelectrode that was covered by Au, *e.g.*, *X* = 100 means the entire surface of the photoelectrode was covered by Au, while *X* = 4 corresponds to only 4% surface coverage, leaving 96% free for light absorption). The morphologies of the different Au-patterned configurations and their surface coverages are shown in Fig. 2(a). It can be seen that with the increase in Au-pattern density, a larger portion of the Si/TiO_2 surface was covered, varying between 0.5% to 50%. Fig. 2(b) shows the influence of the Au-pattern coverage on the photocurrent density and onset potential for the Si/TiO_2/Au-*X* photoelectrodes. It can be that

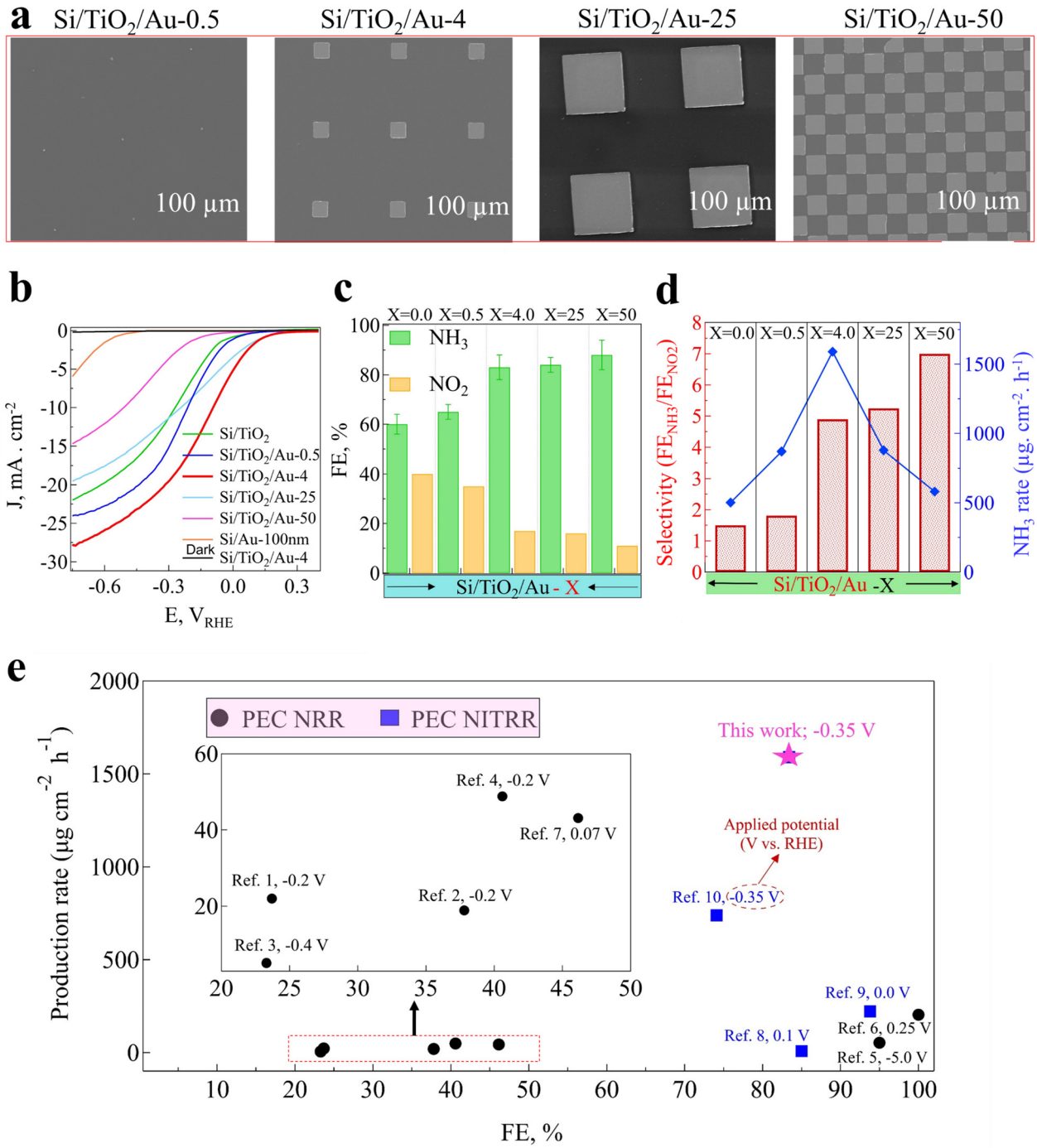

Fig. 2 (a) SEM images of Au pattern with different pattern densities on the surface of Si/TiO_2 substrate, (b) *J*–*V* curves for photocathodes with different patterns in 0.5 M NO_3^- and 1.0 M KOH (pH 14), (c) FE%s for NH_3, and NO_2^- for photocathodes with different Au-pattern densities, (d) selectivity and NH_3 production rate for different Au-pattern densities at −0.35 V *vs.* RHE after 2 h in 1.0 M KOH and 0.5 M NO_3^-, (e) NH_3-production rate *vs.* FE (%), comparison of the current research with previous studies for PEC NH_3 production, for more information see ESI,† Table S1 and the references in the supporting file.

the photocurrent density was improved for Si/TiO_2/Au-0.5 compared to that of Si/TiO_2, and was a maximum for Si/TiO_2/Au-4. As shown in Fig. 2(b), the photoelectrodes with a higher density of Au patterns (*e.g.*, Si/TiO_2/Au-25 and Si/TiO_2/Au-50) showed reduced photocurrent densities due to the decreased carrier generation by Si because of the light blockage by the Au pattern (ESI,† Fig. S16). The roles of the Au-pattern configurations on the FE of NH_3 and NO_2^- and on the selectivity of NH_3 are shown in Fig. 2(c) and (d). As shown in Fig. 2(c), the NH_3 FE increased with increasing the Au-pattern density, reaching a maximum value of 89% NH_3 FE for Si/TiO_2/Au-50, while the FE of NO_2^- continuously decreased to 11%. In contrast, the

NH_3-production rate was maximized for the 4% Au-pattern photoelectrode (Si/TiO_2/Au-4) with an average of 1590 ± 40 μg cm^{-2} h^{-1} (Fig. 2(d)). This obtained NH_3-production rate is competitive among other reported PEC NO_3^--conversion rates for silicon photocathodes used in PEC NH_3 production (ESI,† Table S1).

Although the NH_3 FE and FE_{NH_3}/FE_{NO_2} were increased to 88% and 7 for Si/TiO_2/Au-50, respectively, the NH_3-production rate decreased abruptly to 535 μg cm^{-2} h^{-1}. This could be attributed to the 50% reduction in light absorption by Si/TiO_2/Au-50, consequently leading to deficient electron–hole generation (ESI,† Fig. S16). Next, we quantified the NH_3 concentration using both H-NMR and indophenol blue for different Au patterns in order to compare the reliability of the detection procedure. ESI,† Fig. S17 shows there was a good correlation between both detection methods for quantifying NH_3 in solution.

To shed more light on the interconnected role of light absorption and pattern density, a COMSOL Multiphysics simulation was carried out.[33–35] Here, we calculated the transmitted irradiance and assumed that all transmitted light could participate in charge-carrier generation by p-Si. The detailed computational method presented herein can be found in the "Simulation Method". ESI,† Fig. S18 and S19 demonstrate that the transmitted light was negligible for the Si/TiO_2/Au-100 nm photocathode, leading to the termination of charge-carrier generation by p-Si. However, in the case of Si/TiO_2/Au-4 after light illumination, the onset potential was shifted to 0.15 V *vs.* RHE and the photocurrent density increased to −30 mA cm^{-2} in −0.9 V *vs.* RHE, representing a dramatic change with the dark condition (ESI,† Fig. S20). Furthermore, we checked NH_3 production under light and dark conditions for Si/TiO_2/Au-4 (ESI,† Fig. S21). Under light irradiation, NH_3 production followed the theoretical values, under dark conditions the NH_3 production dropped to nearly zero. The current densities of the Si/TiO_2/Au-4 photoelectrode and the Au electrode alone are shown in ESI,† Fig. S22. The Si/TiO_2/Au-4 photoelectrode exhibited an onset potential of 0.15 V *vs.* RHE for NO_3^- conversion to NH_3, while the Au electrode only showed activity at potentials as low as −0.4 V *vs.* RHE. Furthermore, the absolute reflectances of the Si/TiO_2/Au-*X* (*X* = 0, 0.5, 4, 25, 50, 100) photoelectrodes were measured and are shown in ESI,† Fig. S23. It was observed that Si/TiO_2 reflected about 31.7% of the incident light due to the shiny surface of both the Si and TiO_2 layers. The Au pattern with only 0.5% surface coverage slightly increased the light reflectance, while the Au patterns with 4%, 25%, and 50% coverages increased the incident light proportionally increased the light reflectance in the visible region. Furthermore, 100% surface coverage with Au deposition could reflect 100% of the incident light, effectively acting like a mirror and preventing light transmission into the Si photoelectrode. We next investigated the effect of the applied potential and pH on the activity and NH_3 FE of Si/TiO_2/Au-4 as the most effective photoelectrode for the conversion of NO_3^- to NH_3. All the possible reduction reactions products, including H_2, NH_3, and NO_2 were measured and are shown in ESI,† Fig. S24a at different applied potentials. ESI,† Fig. S25a indicates that at low cathodic applied potentials, NH_3 and NO_2 were the main products on the surface of the Si/Ti/Au-4 photocathode. Although the NH_3 FE at 0.044 V *vs.* RHE was comparable to that at −0.35 V *vs.* RHE, the photocurrent density for the NITRR was much lower, resulting in a lower NH_3-production rate (ESI,† Fig. S24b). At an applied potential of −0.35 V *vs.* RHE, Si/TiO_2/Au-4 showed a maximum NH_3 FE of 83.4 ± 5.6%. With increasing the applied potential to more negative regions (*e.g.*, −1.05 or −1.35 V *vs.* RHE), the HER reaction became more competitive with the NITRR, leading to an FE of about 40% corresponding to H_2 and 30% related to NH_3. One of the most influential operational parameters in the PEC conversion of NO_3^- to NH_3 is the pH of the electrolyte. Consequently, we measured the LSV for Si/TiO_2/Au-4 in three different pH media: acidic (0.5 M H_2SO_4), neutral (0.5 M Na_2SO_4), and alkaline (1.0 M KOH) with the same concentration of NO_3^- (0.5 M KNO_3). As can be seen in ESI,† Fig. S24c and d, the Si/TiO_2/Au-4 photoelectrode showed the highest performance in the alkaline medium. The FEs for the possible products were measured at −0.35 V *vs.* RHE in both acidic and alkaline media, and are shown in ESI,† Fig. S24d. The results indicated that in the acidic medium, HER became a more competitive reaction with the NITRR, while in the alkaline medium, NH_3 was the main product. In the acidic medium, only 25% of the photocurrent was utilized for transforming NO_3^- to NH_3 (FE < 25%), while about 70% of the photocurrent was utilized for the conversion to H_2 gas. In the basic solution (KOH 1.0 M), NO_3^- reduction to NH_3 predominantly occurred, with an NH_3 FE of >88% ± 5%, while the HER reaction was effectively suppressed and no gas bubble were observed on the surface of the photocathode.

The concentration of NO_3^- ions can also influence the performance and NH_3 FE of Si/TiO_2/Au-4, as shown in ESI,† Fig. S25. It could be observed that when the NO_3^- concentration was decreased to 0.1 M (*i.e.*, 5 times less), the current density decreased by 50% compared to that of the 0.5 M concentration (ESI,† Fig. S25a and b). Surprisingly, the Si/TiO_2/Au-4 photoelectrode maintained a high NH_3 FE even at the lower concentration of 0.025 M (ESI,† Fig. S25c). This demonstrates the reliability of the photoelectrode for converting low concentrations of NO_3^- ions into NH_3. Furthermore, we measured the performance of Si/TiO_2/Au-4 in the presence of SO_4^{2-} and NO_3^- with different NO_3^- concentrations at neutral pH (ESI,† Fig. S26). The results indicated that even in the presence of interfering ions, such as SO_4^{2-}, the performance of the photoelectrode was only slightly changed with decreasing the NO_3^- concentration.

2.3. Stability of the Si/TiO_2/Au-4 photoelectrode

In order to investigate the stability of the Si/TiO_2/Au-4 photoelectrode, its top-view surface morphology was analyzed by SEM before and after PEC NO_3^- reduction (Fig. 3(a) and (b)). The SEM images of Si before PEC measurement showed it had a smooth surface, while after immersing the photocathode in the electrolyte and starting the experiments in KOH solution, a 3D

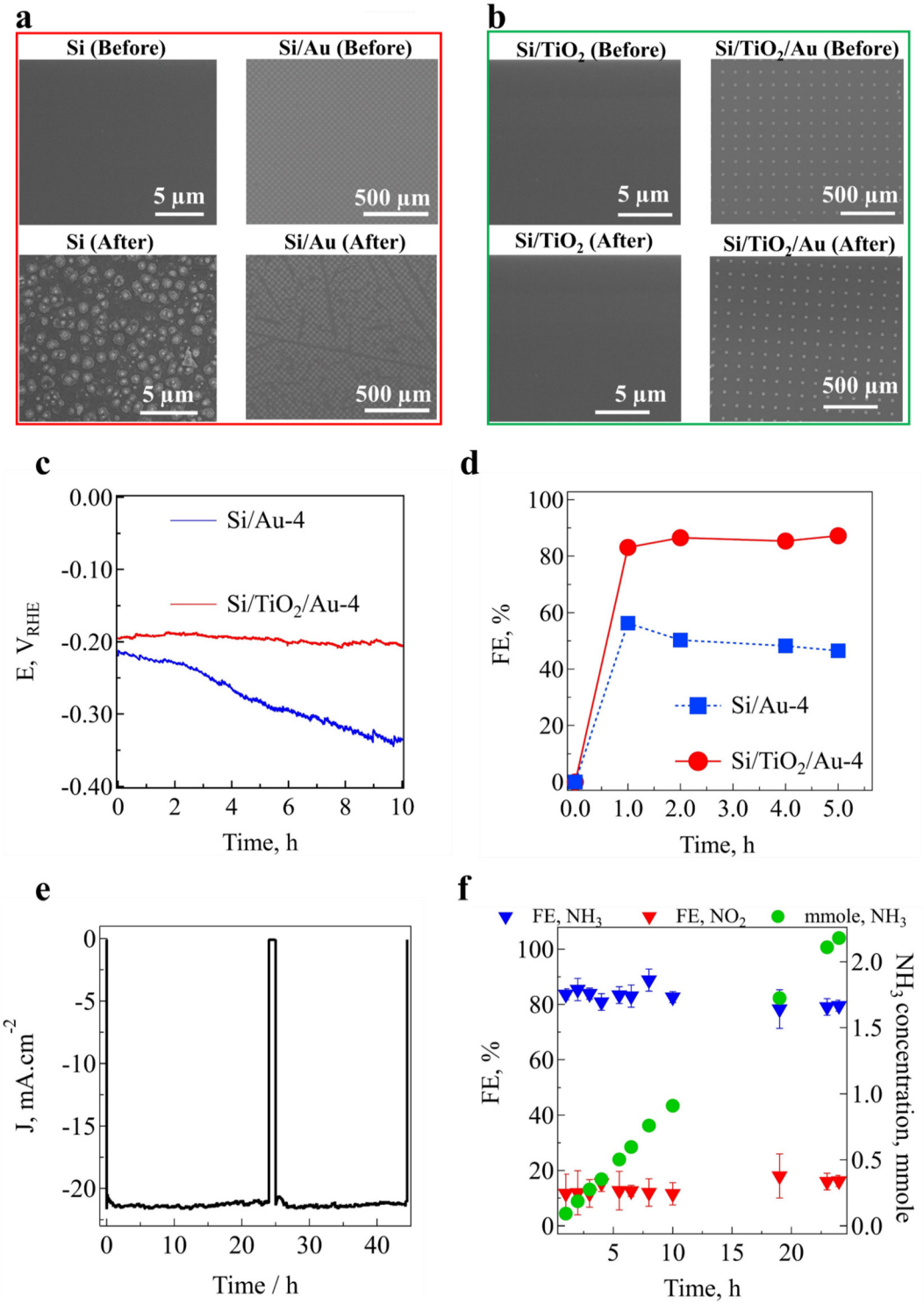

Fig. 3 (a) and (b) Top-view SEM images of photoelectrodes before and after 24 h PEC nitrate (NO_3^-)-reduction measurements, (c) chronopotentiometry (−10 mA cm^{-2}) curves for Si/Au-4 and Si/TiO_2/Au-4 photocathodes in 0.5 M KNO_3 at pH 14, (d) FE (%) for Si/Au-4 and Si/TiO_2/Au-4 photocathodes in 0.5 M KNO_3 at pH = 14 *J*–*V* curves, (e) long-term chronoamperometry stability PEC NO_3^- reduction of Si/TiO_2/Au-4 at −0.35 V *vs.* RHE in 1 M KOH with 0.5 M NO_3^-, and (f) evolution of the FEs and concentration of NH_3 and NO_2^- for 24 h continuous PEC NITRR.

pyramidal structure was observed on the surface of p-Si. This could be attributed to the anisotropic chemical etching of the silicon surface by the KOH aqueous solution, which is a phenomenon that has been known about for a long time.[36–38] After the deposition of a thin TiO_2 protective layer, the Si/TiO_2 photocathode surface remained unchanged and could sustain

its integrity after the PEC NO_3^--reduction experiments (Fig. 3(a) and (b)). Moreover, ESI,† Table S2 summarizes the concentrations of Si, Au, and Ti ions in the catholyte solution, in which the Si concentration reached 11.2 ppm for the Si photoelectrode compared to 0.1 ppm for Si/TiO_2 (ESI,† Fig. S27). Fig. 3(a) shows the detachment of part of the Au pattern in the Si/Au photoelectrode after the PEC experiments, resulting in an increase in Au ion concentration approaching 0.8 ppm. In contrast, the Au patterns remained unchanged on the surface of Si/TiO_2/Au-4 after PEC NO_3^- reduction, and there were no empty or damaged arrays, leading to a very low Au ion concentration of 0.001 ppm. Furthermore, the ICP results in ESI,† Table S2 indicate there was a very low concentration of Ti ions in the catholyte, highlighting the role of the TiO_2 layer as a protective surface. The impact of Au-pattern detachment on the PEC performance and NH_3 FE could also be observed in Fig. 3(c) and (d). Chronopotentiometry measurements were next performed, with a constant −0.2 V *vs.* RHE obtained for the Si/TiO_2/Au-4 photoelectrode, while the voltage continuously decreased for Si/Au to sustain the −10 mA cm^{-2} current density. The NH_3 FE measurement also showed a stable trend for Si/TiO_2/Au-4, while it decreased for the Si/Au-4 photoelectrode. Finally, the long-term stability for PEC NO_3^- reduction to NH_3 was investigated for Si/TiO_2/Au-4 at −0.35 V *vs.* RHE for 44 h (Fig. 3(e)). A stable NO_3^--reduction photocurrent density was recorded, as well as an almost linear increase in NH_3 concentration over time. Fig. 3(f) shows that the NH_3 FE remained constant over 24 h of operation in the range of 83.4 ± 5.6%. Moreover, we investigated the surface morphology of the Si/TiO_2/Au-4 photoelectrode after 44 h continuous operation (ESI,† Fig. S28). Both the AFM and SEM images showed the clean and smooth surface the Au pattern with a height of about 100 ± 5 nm before starting the PEC performance tests. After 44 h PEC conversion of nitrate in the catholyte, the surface of the Au pattern became slightly rough (±10 nm), while the height of the Au pattern stayed in almost the same range.

2.4. Theoretical insight into the NO_3^--reduction mechanism

Next, we sought to gain an atomistic-scale understanding of the NO_3^--reduction reaction using density functional theory (DFT).

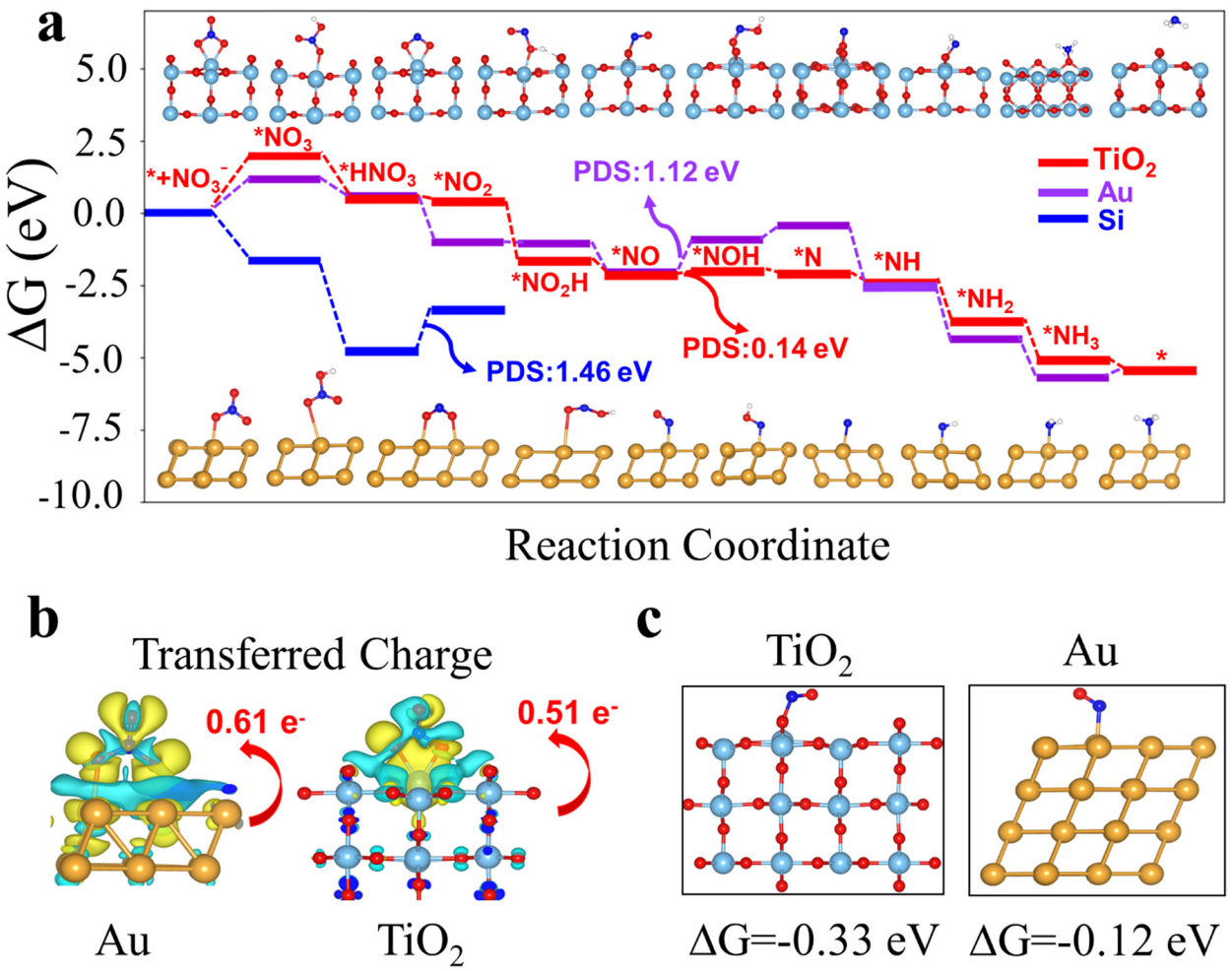

Fig. 4 (a) Free-energy diagram for electrochemical NO_3^- reduction to ammonia (NH_3) on TiO_2(110), Au(111), and Si(111) (b) Charge-density difference for Au(111) and TiO_2(110), where the yellow and cyan colours depict charge accumulation and charge depletion, respectively. (c) Adsorption free-energy changes of NO(g) to *NO on TiO_2(110) and Au(111). Colour code, Ti: light blue, Au: gold, O: red, N: blue, H: white.

The stable structures of rutile TiO_2(110), Au(111), and Si(111) were taken into account in our simulation (more information is provided in the computational method and ESI,† Fig. S29–S32). Electrochemical NO_3^- reaction involves an 8 proton–electron coupled mechanism ($NO_3^- + 6H_2O + 8e^- \rightarrow NH_3 + 9OH^-$), leading to many intermediate steps and by-products, as well as the competing hydrogen evolution reaction (HER). NO_3^- adsorption on the catalyst surface is the primary step for NH_3 synthesis ahead of the deoxygenation/hydrogenation steps. There are two adsorption modes for NO_3^- on the surface in which, namely, one or two metal-to-oxygen (M–O) bonds can be formed. As shown in Fig. 4(a), the preferred configuration for NO_3^- adsorption is on TiO_2, while Au is formed with two and one M–O bond, respectively, and Si strongly adsorbs NO_3^- ($\Delta G = -1.67$ eV) with one M–O bond. The Au surface is a better adsorption site for NO_3^- than TiO_2, according to the free-energy diagram. The charges transferred from the substrate to adsorbed $*NO_3$ on Au and TiO_2 are 0.61 e and 0.51 e (Fig. 4(b)), respectively, which is further evidence of the potential of Au to adsorb NO_3^- ions. The $*NO_3$ protonation step ($*NO_3$ to $*HNO_3$) is downhill for all the catalysts, while on the Si surface the intermediate structure of $*NO_2 + *OH$ is generated. The strong $*NO_3$ adsorption on Si causes an easy first protonation step, but the second step ($*NO_2 + *OH$ to $*NO_2$) is the potential determining step (PDS) with a barrier energy of 1.46 eV, representing the highest barrier among the three catalysts, as well. First principle calculations disclosed that the desorption of $*NO_2$ species on the Au surface requires overcoming a large barrier of 1.8 eV, ensuring subsequent reactions towards the final product (NH_3). The free-energy change of the NO molecule ($NO_{(g)}$ to *NO) on TiO_2 (-0.33 eV) is more negative than on Au (-0.12 eV), as shown in Fig. 4(c), demonstrating a better potential of TiO_2 for the subsequent reactions (*NO, *NOH, *N, *NH, $*NH_2$, $*NH_3$), most of which are exothermic processes. The free-energy change of *NO to *NOH acted as the PDS on TiO_2 with an ultralow limiting potential of -0.14 V, which is much lower than that of Au at -1.12 V. It is worth noting that even employing the DFT+U scheme did not significantly alter the results, in which the free-energy change for the protonation step of *NO to *NOH was downhill as well, with a small change of 0.09 eV for the adsorption energy of NO_3^- on TiO_2.

The suppression of the competing HER reaction is imperative for an efficient NO_3^- reaction. We calculated the adsorption free energy of *H on the catalysts. The ΔG_{*H} ($* + H^+ + e^- \rightarrow *H$) on Au(111) was +0.26 eV, which was about two times larger than the PDS (0.14 eV) of the NITRR (ESI,† Fig. S33), demonstrating that NH_3 was by far the most generated product compared to H_2. Furthermore, the results showed that the ΔG_{*H} on TiO_2 as the main catalyst was 2.39 eV (metal site), indicating that the HER would be strongly suppressed. The more negative limiting potentials of the HER indicate that the NITRR would be the dominant reaction, leading to outstanding selectivity. In addition, protons (H^+) are better nucleophiles than NO_3^- in the electrolyte, resulting in a better adsorption of NO_3^- at the electron-deficient metal centres.

In the first step, both Au and TiO_2 surfaces can adsorb NO_3^-, with the adsorption free energy on Au (1.16 eV) being much lower than on TiO_2 (1.95 eV). Once the reaction is triggered, subsequent reactions can easily proceed on TiO_2 and Au, while NO gas can be chemisorbed on TiO_2 with a low limiting potential of -0.14 V for NH_3 production. In fact, the Au surface is effective at capturing NO_3^- ions and transforming them into *NO species, while TiO_2 mainly catalyzes NO_3^- to NH_3 with a largely reduced onset potential (0.14 eV). The PDS of Si is very high (1.46 eV), which prevents the efficient reduction of NO_3^- to NH_3, aligning with our experimental results. These DFT results demonstrate the synergistic effect of Au and TiO_2 layers for selective NH_3 production from NO_3^- reduction.

3. Conclusion

The synergistic role of Au pattern and TiO_2 layer was elaborated for the PEC conversion of NO_3^- ions into NH_3 using Si photocathodes. The ALD-TiO_2 layer demonstrated multifunctional duties, including chemical etching protection, serving as an adhesion layer for the catalyst/Si interface, and catalyzing NO_3^- reduction to NH_3. The Au pattern facilitated the $2e^-$ RDS of NO_3^- to NO_2^- reduction, resulting in enhanced PEC performance for Si/Au and Si/TiO_2/Au after printing the Au pattern on the electrodes. The ideal pattern density of Au was also investigated by determining the NH_3 production rate and FE for different pattern configurations. The Si/TiO_2/Au-4 photoelectrode, which had a 4% Au-pattern coverage of the Si/TiO_2 surface, demonstrated a high NH_3 production rate of 1590 ± 40 μg_{NH_3} cm^{-2} h^{-1} at -0.35 V *vs.* RHE, which is the highest value reported yet for PEC NH_3 production with silicon photocathodes.

4. Experimental section

4.1. Preparation of p-type silicon

As-supplied p-type boron-doped ⟨100⟩ silicon wafers (p-Si) with a resistivity of 10–20 Ohm m and 525 μm thickness (Atecom Ltd, Taiwan) were utilized as substrates for the fabrication of the photocathode. To remove the oxide layer (SiO_2), the p-Si wafers were immersed in 10% HF aqueous solution just before a thin layer of TiO_2 was deposited using the atomic layer deposition (ALD) technique.

4.2. Atomic layer deposition

A 20 nm TiO_2 layer was coated by ALD (Lucida D100) onto an HF-treated p-Si wafer using a TTiP precursor and H_2O at 150 °C at a flow rate of 6.5 ml min^{-1}. To achieve adequate vapour pressure, the $C_8H_{24}N_4Ti$ was heated to 75 °C. A sequential process was utilized and adjusted for 20 nm deposition of the TiO_2 layer onto the p-Si substrate.

4.3. Photolithography process for the fabrication of Au patterns

The metal frame formation process included the standard photolithography process, metal deposition, and subsequent lift-off. In the photolithography process, the Cr photomask was

designed to make patterns of different sizes and densities (5 × 5 μm, 20 × 20 μm low density, 20 × 20 μm high density, and 75 × 75 μm). The photoresist (PR, AZ5214E, positive) was spin-coated at 4000 rpm for 60 s, followed by soft baking at 95 °C for 60 s. The sample was illuminated by a UV lamp in a mask aligner through a Cr mask with an exposure dose of 90 mJ cm^2. After the exposure, the sample was developed in MIF 300 (metal-ion tree) developer for more than 50 s.[30,31,39]

A 100 nm metallic film was deposited by an e-beam evaporator (KVE-E4000) without rotation at a rate of 0.3 Å s^{-1} to fill the holes of the photoresist patterns. A thin 3 nm layer of Cr was evaporated before the metallic film to increase the adhesion of the metallic layer and TiO_2 frame. Finally, the desired pattern was obtained by lifting off the resist in acetone and by oxygen plasma treatment using a plasma asher system to remove extra PR residue.

In the Si/TiO_2/Au-X photoelectrode, where X is correlated to the percentage of the photoelectrode surface covered by Au: for example, X = 100 means the entire surface is covered by gold, which leads to minimal light absorption because gold typically absorbs light in the visible and near-infrared range. In the case of $0 < X < 100$, as the gold coverage (X) decreases, a larger portion of the surface is exposed, allowing for increased light absorption by the underlying Si material. Finally, for $X = 0$, with no gold coverage, the photoelectrode has maximum light absorption, but the silicon surface is inactive for nitrate conversion to NH_3.

4.4. Characterization

The Si surface and Au pattern morphologies were analyzed by field emission scanning electron microscopy (FE-SEM, S4800, HITACHI) and energy-dispersive X-ray spectroscopy. UV-visible-diffuse reflectance spectroscopy (UV-DRS) was used to measure the reflectance of p-Si and the different patterns on the p-Si substrate using a UV-3600 instrument (Shimadzu). The Si and Au contents in the catholyte solutions were evaluated by inductively coupled plasma optical emission spectrometry (Varian 700-ES).

4.5. Photoelectrochemical nitrogen reduction

The PEC measurements were conducted using a customized H-type cell configuration with a Nafion membrane (Fuel Cell Store) to separate the catholyte and anolyte. The catholyte compartment was equipped with a gas-sealed Ar flow inlet and outlet, and was connected online to a gas chromatography system (GC, X) to detect the evolution of H_2 during the PEC measurements. Additionally, a gas-sealed syringe connection was installed in the catholyte for taking liquid samples for measurement of the NH_3 and NO_2^- concentrations using indophenol blue and Griess protocols, respectively. A potentiostat (IviumStat, Ivium Technologies) was used to collect and analyze the PEC data in a three-electrode system with Hg/HgO (or Ag/AgCl) as the reference electrode, Pt wire as the counter electrode, and Si/Ti/Au photocathodes as the working electrode. To simulate 1 sunlight illumination (100 mW cm^{-2}), a 1.5 G filter was placed in front of a Xe lamp (300 W) and the light intensity was calibrated with a reference certified by NREL, USA. The pH of the electrolyte was adjusted using 1.0 M KOH, 0.5 M H_2SO_4, and K_2SO_4 for obtaining alkaline, acidic, and neutral electrolytes, respectively. Also, 30 ml of electrolyte containing NO_3^- at various concentrations was used in the catholyte for the PEC measurements. Before each measurement, the surface of the photocathodes was scanned by J–V to ensure a stable surface of the Si–Ti–Au photocathodes. The Faraday efficiencies (FEs) for NH_3 and NO_2 and the selectivity for NH_3 were calculated as follows:

$$FE_{NH_3} = \frac{(8 \times F \times C_{NH_3} \times V)}{Q} \quad (4)$$

$$FE_{NO_2} = \frac{(2 \times F \times C_{NO_2} \times V)}{Q} \quad (5)$$

$$\text{Selectivity toward ammonia} = \frac{FE_{NH_3}}{FE_{NO_2}} = \frac{8 \times C_{NH_3}}{2 \times C_{NO_2}} \quad (6)$$

4.6. Ammonia detection process

The ammonia concentration was measured using the well-known indophenol blue spectroscopy method.[7,8] Samples were appropriately diluted and mixed with 1 ml NaOH (1 M) containing 5 wt% salicylic acid and 5 wt% sodium citrate solution. Next, 0.5 ml of 0.05 M NaClO was added to the solution, followed by 0.1 ml sodium nitroferricyanide solution (1.0 wt%). The mixture was kept in the dark for 1 h before being analyzed with a UV-Vis spectrophotometer. The peak absorbance at 655 nm wavelength was recorded, and the concentrations were calculated using a standard concentration–absorbance calibration curve with NH_4Cl solution (ESI,† Fig. S10).

Furthermore, a 500 MHz nuclear magnetic resonance (NMR) spectrometer was used to measure the NH_3 concentration according to a previously reported procedure. After diluting the samples to fall within the detection range, they were mixed with 0.1 ml DMSO. The sample was measured with a Liquid Bruker Avance NMR spectrometer (ESI,† Fig. S11).

4.7. Nitrite-detection process

The NO_2^- concentration was also calculated using a spectroscopy procedure as previously reported.[7,8] Here, a 2.0 g solution of *p*-aminobenzenesulfonamide was dissolved in 50 ml and kept at low temperature ($T < 5$ °C). Another solution was then prepared by mixing 0.1 g ethylenediamine dihydrochloride with 3.94 ml phosphoric acid in 50 ml deionized water. Before the UV-vis measurements, the volumes of the prepared solutions were mixed and kept in the fridge for detection. Then 1.0 ml of the samples was diluted to fall within the detection range, mixed with 2.0 ml 0.5 M H_2SO_4 solution, and then combined with 1 ml of the colour reagent. The peak intensity at 540 nm was measured by UV-vis spectrophotometry (UV-2600). The concentration was calculated using the concentration–absorbance calibration curve fitting equation (ESI,† Fig. S12).

4.8. COMSOL multiphysics simulation

We calculated the transmitted irradiance at the Au/Si and water/Si interfaces. Assuming that all the transmitted light is eventually absorbed in the Si substrate, the transmitted irradiance can be regarded as the absorbed irradiance. The transmitted irradiance I_t can then be written as follows:

$$I_t = \frac{|E_t|^2 \cdot n_{Si}}{|E_0|^2 \cdot n_{water}} \cdot I_0 \quad (7)$$

where E_t and E_0 are the transmitted and incident electric fields, respectively, n_{Si} is the real part of the refractive index of Si, n_{water} is the refractive index of water, and I_0 is the incident irradiance. We set $n_{water} = 1.33$ and I_0 is given by the reference spectral data in 'ASTM G173-03', while $|E_t|^2/|E_0|^2$ can be determined by considering the Fresnel coefficients and multiple reflections.[33] For the Au/Si interface,

$$\frac{|E_t|^2}{|E_0|^2} = \left| \frac{4 n_{water} \tilde{n}_{Au}}{(n_{water} + \tilde{n}_{Au})(\tilde{n}_{Au} + \tilde{n}_{Si}) \exp(-i\tilde{n}_{Au} k_0 h) - (\tilde{n}_{Au} - \tilde{n}_{Si})(\tilde{n}_{Au} - n_{water}) \exp(i\tilde{n}_{Au} k_0 h)} \right|^2. \quad (8)$$

where $\tilde{n}_{Au}$ and $\tilde{n}_{Si}$ are complex refractive indexes of Au and Si, respectively, k_0 is the free-space wavenumber, and h is the Au film thickness. For $\tilde{n}_{Au}$ and $\tilde{n}_{Si}$, we used the previously tabulated data.[35] For the water/Si interface,

$$\frac{|E_t|^2}{|E_0|^2} = \left| \frac{2 n_{water}}{n_{water} + \tilde{n}_{Si}} \right|^2. \quad (9)$$

The simulation for the energy flux $|S_z/S_0|$ distribution was conducted using COMSOL Multiphysics 6.0 at a wavelength of 480 nm where the transmitted irradiance at the water/Si interface is the maximum. The Au film width was scaled down to 1 μm to reduce the computational burden, but to represent the physical implication yet.

4.9. Computational details

The spin-polarized density functional theory (DFT) implemented in the Vienna *ab initio* simulation package (VASP) was used for all the calculations.[40] The Perdew–Burke–Ernzerhof (PBE)[41] functional within the generalized gradient approximation (GGA) was used to model the exchange–correlation interactions, while the van der Waals (vdW) corrections were described by the Tkatchenko–Scheffler (TS) scheme.[42] The projector augmented wave method (PAW) was employed to describe the electron–nucleus interactions. The energy cutoff was 500 eV and at least a 15 Å vacuum space was applied to avoid interactions between adjacent layers in the perpendicular direction to the surface. Nine, four and six layers of rutile TiO_2(110), Au(111), and Si(111) were utilized to model our slab geometries (Fig. S1, ESI†). Among the catalysts, except for the two bottom layers of TiO_2 which were fixed, all other layers were fully relaxed using $2 \times 2 \times 1$, $4 \times 4 \times 1$, and $1 \times 1 \times 1$ Monkhorst–Pack k-point grids for TiO_2(110), Au(111), and Si(111) (a supercell of 96 atoms), respectively. The energy convergence and residual force criteria in the self-consistent field (SCF) were set to 10^{-5} eV and 0.02 eV Å^{-1}, respectively. The Gibbs free energy was calculated based on the computational hydrogen electrode (CHE).[43] The free energy change was calculated by $\Delta G = \Delta E + \Delta ZPE - T\Delta S + \Delta G_U$, where ΔE is the electronic energy difference, ΔZPE is the difference in the zero-point energy, T is the temperature (298.15 K), ΔS is the entropy change, and ΔG_U ($-eU$) is the free energy related to the applied electrode potential, while U and e are the applied potential and the charge of the electron, respectively. The limiting potential (U_L) was employed to evaluate the catalytic activity. Here, U_L was obtained by considering the potential determining step ($U_L = -\Delta G_{PDS}/e$). Since dealing with charged NO_3^- species in periodic DFT calculation is challenging, we chose natural $HNO_{3(g)}$ as the reference value as follows:[44,45]

$$* + HNO_3(g) \rightarrow *NO_3 + H^+ + e^- \quad (10)$$

$$\Delta G_{*NO_3} = G_{*NO_3} - G_{HNO_3} - G_* + 0.5 G_{*H_2} + \Delta G_{correction}$$

where G_*, G_{HNO_3}, G_{*NO_3}, and G_{H_2} are the Gibbs free energy of the substrate, HNO_3, NO_3^- adsorbed on substrates, and H_2 molecules in the gas phase, respectively. In addition, $\Delta G_{correct}$ indicates the correction of the adsorption energy, which is added to eqn (S1) (ESI†) (0.392 eV).[46]

The elementary steps for the NITRR can be described as follows (in adsorbed *NO, N is attached to the metal):

$$* + NO_3^- \rightarrow *NO_3 \quad (11)$$

$$*NO_3 + H^+ + e^- \rightarrow *HNO_3 \quad (12)$$

$$*HNO_3^- + H^+ + e^- \rightarrow *NO_2 + H_2O \quad (13)$$

$$*NO_2 + H^+ + e^- \rightarrow *HNO_2 \quad (14)$$

$$*HNO_2 + H^+ + e^- \rightarrow *NO + H_2O \quad (15)$$

$$*NO + H^+ + e^- \rightarrow *NOH \quad (16)$$

$$*NOH + H^+ + e^- \rightarrow *N + H_2O \quad (17)$$

$$*N + H^+ + e^- \rightarrow *NH \quad (18)$$

$$*NH + H^+ + e^- \rightarrow *NH_2 \quad (19)$$

$$*NH_2 + H^+ + e^- \rightarrow *NH_3 \quad (20)$$

$$*NH_3 \rightarrow NH_{3(g)} \quad (21)$$

Author contributions

A. T. and J.-W. J. conceived and proposed this work. A. T. and J. J. performed and designed the experiments and analysis. M. H. fabricated the Au pattern on Si wafer directed by D. K. J. J. and A. T. measured the PEC performance for NITRR with

quantification of products. A. T., J. J., M. T., and Ch. S. characterised and interpreted the photoelectrodes physiochemical and morphological properties. M. Z. and G. L. performed the DFT calculations and wrote the corresponding section. D. L. conducted the COMSOL Multiphysics simulations directed by D. K. A. T. and J.-W. J. co-wrote the manuscript. M. G. L. revised the manuscript and H.-J. G. performed experiments regarding the effect of light. All authors read and commented on the manuscript.

Data availability

All the experimental data are included in the main text or in the ESI.†

Conflicts of interest

The authors declare no competing interests.

Acknowledgements

This work was supported by the National Research Foundation (NRF; RS-2023-00222006, 2019H1D3A1A01103006, 2022H1D 3A3A01081140, and RS-2023-00257666), as well as the Research Fund (1.240005.01) of the UNIST, sponsored this study (Ulsan National Institute of Science and Technology). A. T. and M. G. L. acknowledges financial support from the European Union (Marie Skłodowska-Curie Actions, 101107294).

References

1 Y. Kojima and M. Yamaguchi, Ammonia as a hydrogen energy carrier, *Int. J. Hydrogen Energy*, 2022, **47**, 22832–22839.
2 B. H. R. Suryanto, *et al.*, Challenges and prospects in the catalysis of electroreduction of nitrogen to ammonia, *Nat. Catal.*, 2019, **2**, 290–296.
3 M. Wang, *et al.*, Can sustainable ammonia synthesis pathways compete with fossil-fuel based Haber–Bosch processes?, *Energy Environ. Sci.*, 2021, **14**, 2535–2548.
4 D. R. MacFarlane, *et al.*, A Roadmap to the Ammonia Economy, *Joule*, 2020, **4**, 1186–1205.
5 J. Zheng, L. Jiang, Y. Lyu, S. P. Jian and S. Wang, Green Synthesis of Nitrogen-to-Ammonia Fixation: Past, Present, and Future, *Energy Environ. Mater.*, 2021, 452–457, DOI: 10.1002/eem2.12192.
6 V. Rosca, M. Duca, M. T. DeGroot and M. T. M. Koper, Nitrogen Cycle Electrocatalysis, *Chem. Rev.*, 2009, **109**, 2209–2244.
7 S. Ghavam, M. Vahdati, I. A. G. Wilson and P. Styring, Sustainable Ammonia Production Processes, *Front. Energy Res.*, 2021, **9**, 1–19.
8 V. Kyriakou, I. Garagounis, A. Vourros, E. Vasileiou and M. Stoukides, An Electrochemical Haber–Bosch Process, *Joule*, 2020, **4**, 142–158.
9 C. Arnaiz del Pozo and S. Cloete, Techno-economic assessment of blue and green ammonia as energy carriers in a low-carbon future, *Energy Convers. Manage.*, 2022, **255**, 115312.
10 P. M. Krzywda, *et al.*, Electroreduction of NO_3- on tubular porous Ti electrodes, *Catal. Sci. Technol.*, 2022, 3281–3288, DOI: 10.1039/d2cy00289b.
11 D. Liu, *et al.*, Photoelectrochemical Synthesis of Ammonia with Black Phosphorus, *Adv. Funct. Mater.*, 2020, **30**, 1–7.
12 N. C. Kani, A. Prajapati and M. R. Singh, Sustainable Routes for Photo-Electrochemical Synthesis of Ammonia Using Various Nitrogen Precursors, *ACS ES&T Eng.*, 2022, **2**, 1080–1087.
13 R. Daiyan, *et al.*, Nitrate reduction to ammonium: From CuO defect engineering to waste NO_x-to-NH_3 economic feasibility, *Energy Environ. Sci.*, 2021, **14**, 3588–3598.
14 H. Okamoto, *et al.*, Effects of annealing conditions on the oxygen evolution activity of a $BaTaO_2N$ photocatalyst loaded with cobalt species, *Catal. Today*, 2019, **354**, 204–210.
15 L. Barrera and R. Bala Chandran, Harnessing Photoelectrochemistry for Wastewater Nitrate Treatment Coupled with Resource Recovery, *ACS Sustainable Chem. Eng.*, 2021, **9**, 3688–3701.
16 A. Tayyebi, *et al.*, Bias-free solar NH_3 production by perovskite-based photocathode coupled to valorization of glycerol, *Nat. Catal.*, 2024, **7**, 510–521.
17 J. Saari, *et al.*, Interface Engineering of TiO_2 Photoelectrode Coatings Grown by Atomic Layer Deposition on Silicon, *ACS Omega*, 2021, **6**, 27501–27509.
18 S. Hu, *et al.*, Amorphous TiO_2 coatings stabilize Si, GaAs, and GaP photoanodes for efficient water oxidation, *Science*, 2014, **344**, 1005–1009.
19 M. Hannula, *et al.*, Improved Stability of Atomic Layer Deposited Amorphous TiO_2 Photoelectrode Coatings by Thermally Induced Oxygen Defects, *Chem. Mater.*, 2018, **30**, 1199–1208.
20 M. Ali, *et al.*, Nanostructured photoelectrochemical solar cell for nitrogen reduction using plasmon-enhanced black silicon, *Nat. Commun.*, 2016, **7**, 1–5.
21 M. Xu, *et al.*, Atomic layer deposition technique refining oxygen vacancies in TiO_2 passivation layer for photoelectrochemical ammonia synthesis, *Compos. Commun.*, 2022, **29**, 101037.
22 H. E. Kim, *et al.*, Photoelectrochemical Nitrate Reduction to Ammonia on Ordered Silicon Nanowire Array Photocathodes, *Angew. Chem., Int. Ed.*, 2022, **61**, e202204117.
23 H. Huang, *et al.*, Lithium-Mediated Photoelectrochemical Ammonia Synthesis with 95% Selectivity on Silicon Photocathode, *ACS Energy Lett.*, 2023, **8**, 4235–4241.
24 J. Zheng, *et al.*, Photoelectrochemical Synthesis of Ammonia on the Aerophilic-Hydrophilic Heterostructure with 37.8% Efficiency, *Chem*, 2019, **5**, 617–633.
25 N. S. Lewis and D. G. Nocera, Powering the planet: Chemical challenges in solar energy utilization, *Proc. Natl. Acad. Sci. U. S. A.*, 2006, **103**, 15729–15735.
26 P. Thangavel, *et al.*, Graphene-nanoplatelets-supported NiFe-MOF: High-efficiency and ultra-stable oxygen electrodes for

sustained alkaline anion exchange membrane water electrolysis, *Energy Environ. Sci.*, 2020, **13**, 3447–3458.
27 J. Li, *et al.*, Efficient Ammonia Electrosynthesis from Nitrate on Strained Ruthenium Nanoclusters, *J. Am. Chem. Soc.*, 2020, **142**, 7036–7046.
28 X. Zhang, *et al.*, Regulating intermediate adsorption and H2O dissociation on a diatomic catalyst to promote electrocatalytic nitrate reduction to ammonia, *Energy Environ. Sci.*, 2024, 6717–6727, DOI: **10.1039/d4ee02747g**.
29 J. M. McEnaney, *et al.*, Electrolyte engineering for efficient electrochemical nitrate reduction to ammonia on a titanium electrode, *ACS Sustainable Chem. Eng.*, 2020, **8**, 2672–2681.
30 G. Choi, *et al.*, Enhanced Terahertz Shielding of MXenes with Nano-Metamaterials, *Adv. Opt. Mater.*, 2018, **6**, 1–6.
31 W. Park, J. Rhie, N. Y. Kim, S. Hong and D. S. Kim, Sub-10 nm feature chromium photomasks for contact lithography patterning of square metal ring arrays, *Sci. Rep.*, 2016, **6**, 1–6.
32 W. Jung and Y. J. Hwang, Material strategies in the electrochemical nitrate reduction reaction to ammonia production, *Mater. Chem. Front.*, 2021, **5**, 6803–6823.
33 C. Schinke, *et al.*, Uncertainty analysis for the coefficient of band-to-band absorption of crystalline silicon, *AIP Adv.*, 2015, **5**, 067168.
34 H. Li, Y. Hu, Y. Yang and Y. Zhu, Theoretical investigation of broadband absorption enhancement in a-Si thin-film solar cell with nanoparticles, *Sol. Energy Mater. Sol. Cells*, 2020, **211**, 110529.
35 S. Babar and J. H. Weaver, Optical constants of Cu, Ag, and Au revisited, *Appl. Opt.*, 2015, **54**, 477.
36 H. Tanaka, S. Yamashita, Y. Abe, M. Shikida and K. Sato, Fast etching of silicon with a smooth surface in high temperature ranges near the boiling point of KOH solution, *Sens. Actuators, A*, 2004, **114**, 516–520.
37 E. Van Veenendaal, K. Sato, M. Shikida and J. Van Suchtelen, Micro-morphology of single crystalline silicon surfaces during anisotropic wet chemical etching in KOH: Velocity source forests, *Sens. Actuators, A*, 2001, **93**, 232–242.
38 R. Rao, J. E. Bradby and J. S. Williams, Patterning of silicon by indentation and chemical etching, *Appl. Phys. Lett.*, 2007, **91**, 1–4.
39 H. S. Kim, *et al.*, Phonon-Polaritons in Lead Halide Perovskite Film Hybridized with THz Metamaterials, *Nano Lett.*, 2020, **20**, 6690–6696.
40 D. Joubert, From ultrasoft pseudopotentials to the projector augmented-wave method, *Phys. Rev. B: Condens. Matter Mater. Phys.*, 1999, **59**, 1758–1775.
41 J. P. Perdew, K. Burke and M. Ernzerhof, Generalized gradient approximation made simple, *Phys. Rev. Lett.*, 1996, **77**, 3865–3868.
42 A. Tkatchenko and M. Scheffler, Accurate molecular van der Waals interactions from ground-state electron density and free-atom reference data, *Phys. Rev. Lett.*, 2009, **102**, 6–9.
43 J. K. Nørskov, *et al.*, Origin of the overpotential for oxygen reduction at a fuel-cell cathode, *J. Phys. Chem. B*, 2004, **108**, 17886–17892.
44 J. X. Liu, D. Richards, N. Singh and B. R. Goldsmith, Activity and Selectivity Trends in Electrocatalytic Nitrate Reduction on Transition Metals, *ACS Catal.*, 2019, **9**, 7052–7064.
45 S. Guo, *et al.*, Insights into Nitrate Reduction over Indium-Decorated Palladium Nanoparticle Catalysts, *ACS Catal.*, 2018, **8**, 503–515.
46 H. Niu, *et al.*, Theoretical Insights into the Mechanism of Selective Nitrate-to-Ammonia Electroreduction on Single-Atom Catalysts, *Adv. Funct. Mater.*, 2021, **31**, 2008533.